



The Mass Inflow and Outflow Rates of the Milky Way

Andrew J. Fox¹, Philipp Richter², Trisha Ashley³, Timothy M. Heckman⁴, Nicolas Lehner⁵, Jessica K. Werk⁶,
Rongmon Bordoloi⁷, and Molly S. Peeples^{3,4}

¹ AURA for ESA, Space Telescope Science Institute, 3700 San Martin Drive, Baltimore, MD 21218, USA; afox@stsci.edu

² Institut für Physik und Astronomie, Universität Potsdam, Haus 28, Karl-Liebknecht-Str. 24/25, D-14476, Potsdam, Germany

³ Space Telescope Science Institute, 3700 San Martin Drive, Baltimore, MD 21218, USA

⁴ Department of Physics and Astronomy, Johns Hopkins University, 3400 N. Charles Street, Baltimore, MD 21218, USA

⁵ Department of Physics, University of Notre Dame, 225 Nieuwland Science Hall, Notre Dame, IN 46556, USA

⁶ Department of Astronomy, University of Washington, Box 351580, Seattle, WA 98195, USA

⁷ Department of Physics, North Carolina State University, 2401 Stinson Drive, Raleigh, NC 27695, USA

Received 2019 August 7; revised 2019 August 27; accepted 2019 August 29; published 2019 October 11

Abstract

We present new calculations of the mass inflow and outflow rates around the Milky Way (MW), derived from a catalog of ultraviolet metal-line high-velocity clouds (HVCs). These calculations are conducted by transforming the HVC velocities into the Galactic standard of rest (GSR) reference frame, identifying inflowing ($v_{\text{GSR}} < 0 \text{ km s}^{-1}$) and outflowing ($v_{\text{GSR}} > 0 \text{ km s}^{-1}$) populations, and using observational constraints on the distance, metallicity, dust content, covering fractions, and total silicon column density of each population. After removing HVCs associated with the Magellanic Stream and the Fermi Bubbles, we find inflow and outflow rates in cool ($T \sim 10^4 \text{ K}$) ionized gas of $dM_{\text{in}}/dt \gtrsim (0.53 \pm 0.23)(d/12 \text{ kpc})(Z/0.2Z_{\odot})^{-1} M_{\odot} \text{ yr}^{-1}$ and $dM_{\text{out}}/dt \gtrsim (0.16 \pm 0.07)(d/12 \text{ kpc})(Z/0.5Z_{\odot})^{-1} M_{\odot} \text{ yr}^{-1}$. The apparent excess of inflowing over outflowing gas suggests that the MW is currently in an inflow-dominated phase, but the presence of substantial mass flux in both directions supports a Galactic fountain model, in which gas is constantly recycled between the disk and the halo. We also find that the *metal flux* in both directions (in and out) is indistinguishable. By comparing the outflow rate to the Galactic star formation rate, we present the first estimate of the mass loading factor (η_{HVC}) of the disk-wide MW wind, finding $\eta_{\text{HVC}} \gtrsim (0.10 \pm 0.06)(d/12 \text{ kpc})(Z/0.5Z_{\odot})^{-1}$. Including the contributions from low- and intermediate-velocity clouds and from hot gas would increase these inflow and outflow estimates.

Unified Astronomy Thesaurus concepts: Circumgalactic medium (1879); Milky Way Galaxy fountains (1055); Milky Way Galaxy (1054); Galactic winds (572); Milky Way evolution (1052); Galaxy accretion (575); High-velocity clouds (735)

1. Introduction

It has long been known that the Milky Way (MW) accretes gas from its surroundings (Oort 1969), allowing it to sustain its star formation over long ($\sim \text{Gyr}$) timescales (Larson et al. 1980). In turn, this stellar activity drives gas back into the halo of the Galaxy through stellar winds and supernova feedback. Star formation is thus regulated by a symbiotic relationship between inflow and outflow, in which inter-dependent gas flows play an important role in the baryon cycle (Putman et al. 2012; Tumlinson et al. 2017). Observationally characterizing the Galactic mass inflow and outflow rates is of high importance for validating this picture. Studying gas flows around the MW (as opposed to external galaxies) offers several key advantages include proximity, abundance of data, and knowledge of nearby Galactic structure.

Ultraviolet (UV) absorption-line studies are particularly powerful for inflow and outflow studies due to their sensitivity and ability to trace multiple interstellar medium (ISM) gas phases. To identify inflowing and outflowing UV absorbers, foreground components associated with the Galactic ISM need to be removed. Traditionally, this is achieved by classifying interstellar UV absorbers into three populations using their velocity relative to the local standard of rest (LSR): low-velocity clouds (LVCs, $|v_{\text{LSR}}| < 40 \text{ km s}^{-1}$), intermediate-velocity clouds (IVCs, $40 < |v_{\text{LSR}}| < 90 \text{ km s}^{-1}$), and high-velocity clouds (HVCs, $|v_{\text{LSR}}| > 90 \text{ km s}^{-1}$). HVCs are moving too fast for co-rotation with the Galactic disk, and instead represent inflowing or outflowing gas. As such, they are direct

tracers of accretion and feedback and have well-characterized neutral and ionized gas properties (Wakker & van Woerden 1997; Sembach et al. 2003; Collins et al. 2009; Shull et al. 2009; Lehner & Howk 2011; Lehner et al. 2012; Herenz et al. 2013; Fox et al. 2014; Richter 2017).

In this paper, we present new calculations of the mass inflow and outflow rate represented by HVCs, using a new kinematic distinction into inflowing and outflowing populations. This allows us to trace the circulation of gas and metals and hence to derive the *net* inflow rate, the metal flow rates, and the mass loading factor of the outflowing gas, all of which have not been derived before. The paper is structured as follows. In Section 2 we present the equations used to derive the HVC masses and mass flow rates. In Section 3 we describe the adopted values of HVC properties used to evaluate the flow-rate equations, and quantify their uncertainties. In Section 4 we discuss our results and their astrophysical implications. The Appendix describes the propagation of errors through our analysis.

2. Derivation of HVC Mass and Mass Flow Rate

Following earlier work (Wakker et al. 2008; Shull et al. 2009; Lehner & Howk 2011; Lehner et al. 2012; Fox et al. 2014; R17), we derive the gas mass and mass flow rates of HVCs from UV metal-line absorption measurements. The principal difference between our new calculations and earlier work is that we split the HVC population into inflowing and

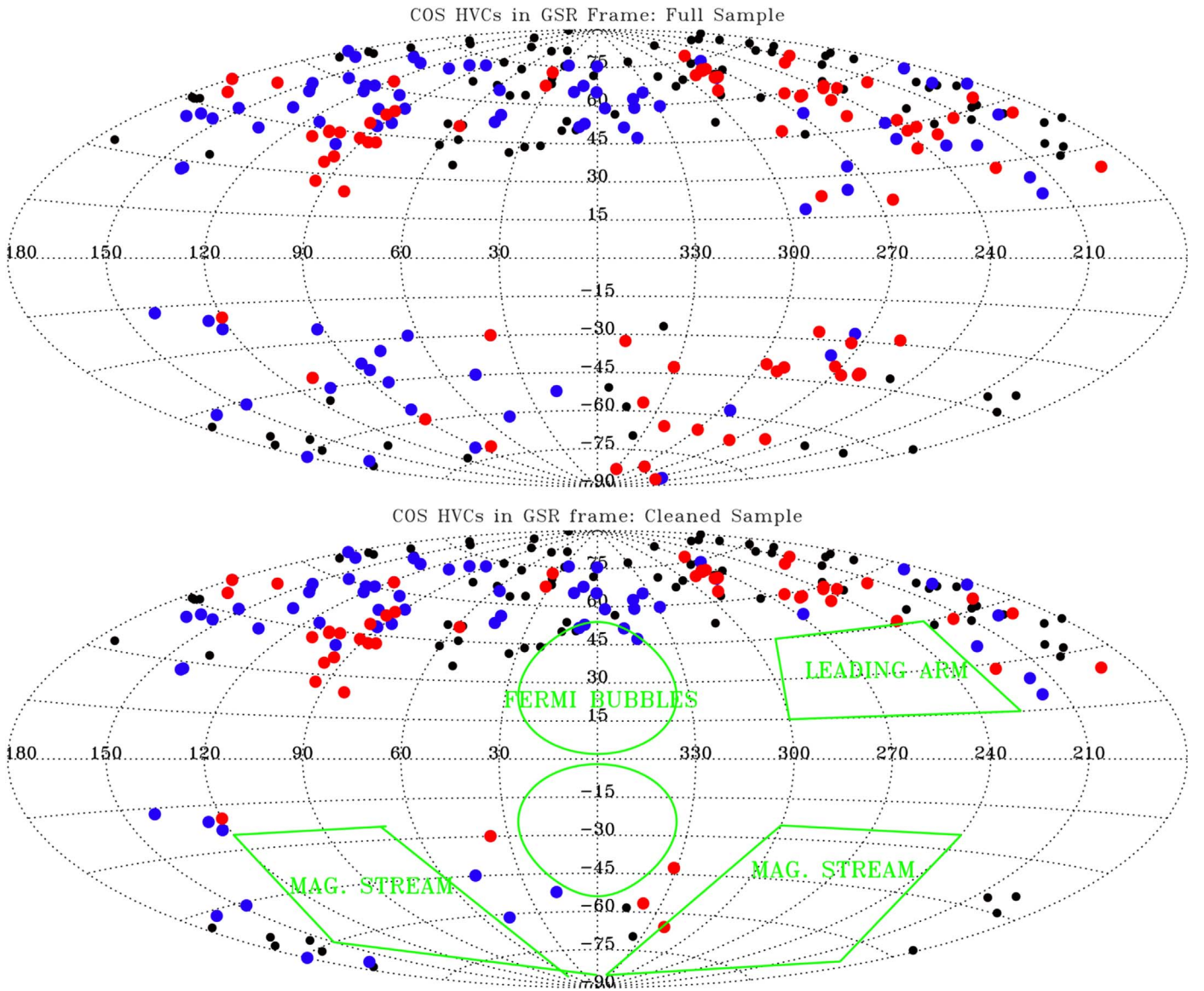


Figure 1. Top: all-sky map in Galactic coordinates of the HVCs in the R17 sample, color coded by their GSR velocity. Inflowing ($v_{\text{GSR}} < 0 \text{ km s}^{-1}$) HVCs are shown in blue, outflowing ($v_{\text{GSR}} > 0 \text{ km s}^{-1}$) HVCs are shown in red, and sightlines with no HVCs detections are shown in black. Bottom: same as the top, but showing the cleaned sample, i.e., with sightlines passing through the Magellanic Stream, Leading Arm, and Fermi Bubbles removed. The outline of these structures is shown in green. Cleaning the sample reduces the sample size, but only slightly reduces the covering fractions.

outflowing components, and conduct the analysis separately for each subset.

We begin with the R17 HVC catalog of 187 metal-line HVCs detected in 270 extragalactic sightlines surveyed with the Cosmic Origins Spectrograph (COS; Green et al. 2012) on the *Hubble Space Telescope* (HST). All 187 HVCs are securely detected, meaning they are present at $>4\sigma$ significance in at least two metal-line transitions (typically Si II $\lambda 1260, 1193, 1190, 1304$, Si III $\lambda 1206$, or C II $\lambda 1334$). The sightlines are spread fairly evenly across the northern and southern Galactic hemispheres at $|b| > 15^\circ$, and also show an approximate east-west symmetry (see Figure 1). By definition, the HVCs are selected in the LSR reference frame, all having either $v_{\text{LSR}} < -90 \text{ km s}^{-1}$ or $v_{\text{LSR}} > 90 \text{ km s}^{-1}$. R17 assessed the presence of sample biases, and found that while some signal-to-noise ratio-related and target-selection biases inevitably exist, these are likely to be minor compared to the other systematics, such as the velocity cutoff used to select HVCs.

First we transform the HVC velocities from the LSR reference frame to the Galactic standard of rest (GSR), to remove the effect of Galactic rotation,

$$v_{\text{GSR}} = v_{\text{LSR}} + 240 \sin l \cos b \text{ km s}^{-1}, \quad (1)$$

where l and b are the Galactic longitude and latitude of the sightline, respectively, and we adopt the rotation velocity at the solar circle of $240 \pm 8 \text{ km s}^{-1}$ from Reid et al. (2014), based in interferometric measurements. We show the sky distribution of the HVC population in the GSR reference frame in the top panel of Figure 1, color coded into inflowing ($v_{\text{GSR}} < 0 \text{ km s}^{-1}$) and outflowing ($v_{\text{GSR}} > 0 \text{ km s}^{-1}$) components. Note that while there is structure in the gas distribution, inflowing and outflowing clouds are often found close together in the same regions of the sky.

Next, we produce a cleaned sample by removing HVCs that are associated with the Magellanic Stream and its Leading

Table 1
Covering Fractions of Inflowing and Outflowing HVCs

Population	$f_{\text{sky,raw}}^a$	$f_{\text{sky,clean}}^a$	$\langle v_{\text{GSR}} \rangle^b$ (km s ⁻¹)	$\langle \log N_{\text{H}} \rangle^c$ (N in cm ⁻²)
Inflowing	0.39 ± 0.03 (106/270)	0.36 ± 0.03 (75/211)	-101 ± 10	18.93 ± 0.06
Outflowing	0.30 ± 0.03 (81/270)	0.25 ± 0.03 (52/211)	+89 ± 12	18.62 ± 0.08

Notes.

^a Sky covering fraction of the raw (R17) and cleaned (non-Magellanic, non-Fermi Bubble) HVC sample. Errors are based on the Wilson score interval.

^b Mean GSR velocity with its standard error.

^c Mean total hydrogen column density from Equation (2) with its standard error, assuming a metallicity of 20% solar for the inflowing gas and 50% solar for the outflowing gas. Value does not account for potential saturation of Si III $\lambda 1206$.

Table 2
HVC Masses, Mass Flow Rates, and Mass Loading Factors

Distance (kpc)	M_{in} (10 ⁷ M _⊙)	M_{out} (10 ⁷ M _⊙)	dM_{in}/dt (M _⊙ yr ⁻¹)	dM_{out}/dt (M _⊙ yr ⁻¹)	dM_{net}/dt (M _⊙ yr ⁻¹)	η_{HVC}^a
5	1.1 ± 0.5	0.4 ± 0.2	-0.22 ± 0.09	0.07 ± 0.03	-0.15 ± 0.09	0.04 ± 0.02
10	4.2 ± 1.7	1.4 ± 0.6	-0.44 ± 0.19	0.13 ± 0.06	-0.31 ± 0.20	0.08 ± 0.05
12	6.1 ± 2.5	2.1 ± 0.9	-0.53 ± 0.23	0.16 ± 0.07	-0.37 ± 0.24	0.10 ± 0.06
15	9.6 ± 4.0	3.3 ± 1.5	-0.66 ± 0.28	0.20 ± 0.09	-0.46 ± 0.29	0.12 ± 0.29

Notes. All values are calculated using Equations (3)–(7), for four assumed distances, chosen to bracket observations, and using 20% solar metallicity for the inflow and 50% solar metallicity for the outflow. Negative flow rates denote infall, so the net flux is inward for all distance cases.

^a $\eta_{\text{HVC}} = (dM_{\text{out}}/dt)/\text{SFR}$ with an SFR of 1.65 M_⊙ yr⁻¹ (Liquia & Newman 2015).

Arm, as these structures are much more distant than the general HVC population (Brüns et al. 2005; Nidever et al. 2008; D’Onghia & Fox 2016). This is achieved by cross-matching the R17 sample with the Fox et al. (2014) catalog of Stream absorbers, which covers sightlines within 30° of the 21 cm emission from the Stream, and then removing matched sightlines from the sample. We also remove several sightlines passing through the Fermi Bubbles (Bordoloi et al. 2017; Karim et al. 2018), as the HVCs in these directions are thought to trace a nuclear wind and so are distinct from the general HVC population.

We then calculate the total (neutral plus ionized) hydrogen column density N_{H} in cool gas ($T \approx 10^4$ K) in each HVC using the silicon lines as a proxy, by summing over the observed ionization states of Si and then correcting for metallicity and dust:

$$N_{\text{H}} = N(\text{H I}) + N(\text{H II}) = \frac{N(\text{Si II}) + N(\text{Si III})}{(\text{Si/H})(10^{[\text{Si/Zn}]})}, \quad (2)$$

where (Si/H) is the gas-phase silicon abundance and the [Si/Zn] term quantifies the level of dust depletion, as Si depletes onto dust grains but Zn is largely undepleted (Jenkins 2009; Tchernyshov et al. 2015). The ionic column densities are apparent optical depth measurements of Si II (based on $\lambda 1260$, 1190, 1193, 1304, 1526) and Si III $\lambda 1206$ (see Table A.4 in R17). Note that this method does not account for metal atoms locked in unobserved ionization states; it is based solely on the observed column densities of the cool-gas tracers Si II and Si III.

Our calculations adopt a two-component spherical-shell model, in which inflowing and outflowing HVCs exist at a uniform distance from the disk with different covering fractions (corrections can be made for ellipsoidal or cylindrical geometries, though these are minor; Richter et al. 2017). In this model the total gas mass contained in HVCs, M , is formed

by combining the mean total hydrogen column $\langle N_{\text{H}} \rangle$ with the measured HVC sky covering fraction f_{sky} and mean HVC distance $\langle d \rangle$. This calculation can be done separately for the inflowing and outflowing populations:

$$M_{\text{in}} = 1.4 m_{\text{H}} f_{\text{sky,in}} \langle N_{\text{H,in}} \rangle 4\pi d^2 \quad \text{and} \quad (3)$$

$$M_{\text{out}} = 1.4 m_{\text{H}} f_{\text{sky,out}} \langle N_{\text{H,out}} \rangle 4\pi d^2, \quad (4)$$

where m_{H} is the mass of the hydrogen atom, the factor 1.4 accounts for the mass in helium and metals, and the covering fractions are assumed to be independent of d . Each of the terms on the right-hand side of Equations (3) and (4) can be directly constrained by observations.

Finally, we combine the gas mass estimates with the mean flow velocities $\langle v_{\text{in}} \rangle$ and $\langle v_{\text{out}} \rangle$ to derive the mass flow rates dM/dt for the inflowing and outflowing HVC populations.

$$dM_{\text{in}}/dt = M_{\text{in}} \langle v_{\text{in}} \rangle / d \quad \text{and} \quad (5)$$

$$dM_{\text{out}}/dt = M_{\text{out}} \langle v_{\text{out}} \rangle / d. \quad (6)$$

The difference between the inflow rate and the outflow rate gives the *net* inflow rate, and the ratio of the mass outflow rate to the star formation rate (SFR) gives the HVC mass loading factor, η_{HVC} , which quantifies the effectiveness of stellar feedback in driving and accelerating the outflow.

$$\eta_{\text{HVC}} = \frac{dM_{\text{out}}/dt}{\text{SFR}}. \quad (7)$$

3. Adopted Values for HVC Parameters

In this section we describe and justify the choice of HVC parameters adopted in the mass flow-rate calculations, and quantify their uncertainties. The covering fractions for the inflowing and outflowing HVC populations are given in Table 1, together with their mean GSR velocities and mean total hydrogen column densities. The resulting values for the

HVC masses, mass flow rates, and mass loading factors (with errors) calculated using Equations (3)–(7) are given in Table 2.

3.1. Covering Fraction

The measured sky covering fractions for *inflowing* HVCs are $39\% \pm 3\%$ (106/270) in the full sample and $36\% \pm 3\%$ (75/211) in the cleaned sample. For *outflowing* HVCs, the covering fractions are $30\% \pm 3\%$ (81/270) in the full sample and $25\% \pm 3\%$ (52/211) in the cleaned sample. The errors here reflect the Wilson score interval. Although the cleaned sample is smaller in size, particularly in the South where most Magellanic gas resides, the covering fractions are only slightly reduced by the sample-cleaning process (see Figure 1), because cleaning removes some directions with nondetections as well as detections. The total sky covering fraction $f_{\text{sky,total}} = f_{\text{sky,in}} + f_{\text{sky,out}} = 69\% \pm 4\%$ for the full sample and $61\% \pm 4\%$ for the cleaned sample, in good agreement with values measured in previous UV HVC surveys: Lehner et al. (2012) report $\approx 68\%$, Shull et al. (2009) report $81\% \pm 5\%$ for a Si III survey, and Sembach et al. (2003) report 58% for an O VI survey. The Si III and O VI surveys have different values because they have differing sensitivities and only require a detection in a single absorption line, whereas R17 and Lehner et al. (2012) require a detection in at least two lines. For comparison, the global 21 cm HVC sky covering fraction is 37% down to $N(\text{H I}) = 7 \times 10^{17} \text{ cm}^{-2}$ (Murphy et al. 1995). The much higher covering fraction in the UV surveys is due to their higher sensitivity: UV HVCs are sensitive to gas down to $\log N(\text{H I}) \sim 14$ (Fox et al. 2006), depending on data quality and metallicity.

The cleaned sample is largely (but not completely) contained in the northern hemisphere, because so much Magellanic gas is removed in the south. If we restrict our analysis to the northern hemisphere only, we find a cleaned covering fraction of $33\% \pm 3\%$ for inflowing HVCs and $25\% \pm 3\%$ for outflowing HVCs, very close to the values obtained from the combined (N+S) sample. Thus we conclude there is no evidence for bias from using a predominantly northern sample, and we proceed with the covering fractions from the combined (N+S) sample. The *nondetections* are distributed across the northern and southern hemispheres, and across the east and west. However, there is some structure in their distribution, with clusters of nondetections found in three regions (see Figure 1): one in the far north at $|b| > 75^\circ$, one in the north at $30 < b < 45^\circ$, $0 < l < 60^\circ$ (east of the Fermi Bubble), and one in the south at $30 < b < 45^\circ$, $0 < l < 60^\circ$ (west of the Magellanic Stream). These indicate that the HVC sky distribution is patchy, as discussed in earlier surveys (Sembach et al. 2003; Fox et al. 2006; Lehner et al. 2012; R17).

3.2. Metallicity

We adopt a 20% solar metallicity for the inflowing gas, $(\text{Si}/\text{H})_{\text{in}} = 0.2(\text{Si}/\text{H})_{\odot}$, based on the observed metallicities of the infalling HVC Complex C (Wakker et al. 1999; Gibson et al. 2001; Richter et al. 2001a; Collins et al. 2003; Tripp et al. 2003; Shull et al. 2011). Fox et al. (2004) updated all the Complex C metallicity measurements onto a common solar abundance scale, and found a mean value of $20\% \pm 4\%$ solar, so we adopt a 20% (4/20) error. We adopt a 50% solar metallicity for the outflowing gas, $(\text{Si}/\text{H})_{\text{out}} = 0.5(\text{Si}/\text{H})_{\odot}$, as seen in the Smith Cloud (Fox et al. 2016), one of the only examples of a metal-enriched (and therefore Galactic in origin)

HVC (see also Zech et al. 2008). We note there are fewer metallicity measurements for outflowing HVCs than for inflowing HVCs. Nonetheless, expectations from theory are that outflowing gas should be metal-enriched, particularly if driven out by feedback from star formation. Furthermore, IVCs are observed to show ≈ 0.5 –1 solar metallicities, indicating that metal-enriched gas exists at lower velocities closer to the disk (Richter et al. 2001a; Wakker 2001; Richter 2017).

3.3. Dust Depletion

For the dust depletion, we adopt an average Si depletion $[\text{Si}/\text{Zn}] = -0.26 \pm 0.14$ measured in MW halo clouds from Sembach & Savage (1996), taken to be applicable to HVCs. This has the effect of increasing the total HVC mass by a factor of 1.8. The presence of dust in HVCs is supported by the detection of far-IR emission from Complex C (Miville-Deschênes et al. 2005), the detection of molecular hydrogen in the Magellanic Stream (Richter et al. 2001b), as H_2 forms on the surface of dust grains, and by UV depletion measurements of the Stream’s chemical composition (Fox et al. 2013). However, IR emission studies of other HVCs found no evidence for dust (Williams et al. 2012; Saul et al. 2014), so the average amount of dust in the HVC population is unknown, and could be small. As such, the dust correction factor of 1.8 is uncertain. We estimate an error of 38% using the dispersion in $[\text{Si}/\text{Zn}]$ in halo clouds (Sembach & Savage 1996).

3.4. Distances

For the HVC distances, we consider four values: 5, 10, 12, and 15 kpc. These values bracket the observed values of both *statistical* HVC distances (Lehner & Howk 2011), which are derived from the similar incidence rates of HVCs toward stars and toward AGN, and *individual* HVC distances (Wakker 2001; Thom et al. 2008; Wakker et al. 2008; Lehner & Howk 2010; Smoker et al. 2011; Richter et al. 2015; Peek et al. 2016), which are based on the detection of HVCs in absorption toward stellar targets at known distance. Both methods find HVC distances in the range ≈ 5 –15 kpc (not including the Magellanic Stream). Lehner & Howk (2011) report a mean value $\langle d \rangle = 12 \pm 4$ kpc, so we adopt this as our nominal distance with a 33% uncertainty ($=4/12$).

3.5. Galactic Star Formation Rate

For the Galactic SFR, published measurements range from 0.68 to $1.45 M_{\odot} \text{ yr}^{-1}$ (Robitaille & Whitney 2010), $1.65 \pm 0.19 M_{\odot} \text{ yr}^{-1}$ (Liquia & Newman 2015), $1.9 \pm 0.4 M_{\odot} \text{ yr}^{-1}$ (Chomiuk & Povich 2011), to $3.8 \pm 2.2 M_{\odot} \text{ yr}^{-1}$ (Diehl et al. 2006), where the differences in part reflect the choice of initial mass function adopted. For example, changing a Kroupa IMF to a Salpeter IMF would increase the derived SFR by a factor of 1.4. We adopt the recent Liquia & Newman (2015) value, though with a larger uncertainty to reflect the 40% IMF error, i.e., $1.7 \pm 0.7 M_{\odot} \text{ yr}^{-1}$. This propagates to the error on the mass loading factor.

3.6. Velocity Limit, Ionization, and Saturation Effects

For several reasons, the HVC inflow and outflow rates calculated using Equations (1)–(6) are lower limits on the true inflow and outflow rates. First, much of the MW halo gas is unobservable in UV absorption because any gas moving at low

velocities blends with the strong foreground ISM absorption. Zheng et al. (2015) used simulations to show that approximately half of the halo gas mass is unobservable because of this effect (see also Qu & Bregman 2019; Zheng et al. 2019), so we should keep in mind that our calculations only refer to gas at HVC velocities. Second, our total hydrogen column density calculations have not accounted for mass in Si IV or unobserved higher ionization states of silicon. We do not include Si IV because the metallicity in the high-ion phase is unknown, and could be different than in the low-ion phase. Any hot ($T > 10^6$ K) outflowing gas is not detectable in UV observations, but according to simulations could bear a substantial fraction of the mass budget (e.g., Fielding et al. 2018; Kim & Ostriker 2018). Third, some unresolved saturation may exist in Si III $\lambda 1206$, a strong line that is often observed to be saturated in HVCs (Collins et al. 2009; Shull et al. 2009; R17). Above $\log N(\text{Si III}) = 12.53$, the optical depth at line center becomes >1 for a line width $b = 10 \text{ km s}^{-1}$, and so saturation becomes potentially important. Si III contributes a large fraction of the total silicon mass because it is often the dominant ionization stage of Si, so saturation of Si III will affect the total Si column. Accounting for each of these effects would serve to increase $\langle N_{\text{H}} \rangle$ and therefore the mass flow rates. Finally, the HVC mass flow rates presented here do not include (by design) the Magellanic Stream and Leading Arm or the Fermi Bubbles, as these structures are physically unrelated to the remaining HVC population. The Stream represents an a much larger inflow rate of $\approx 3\text{--}7 M_{\odot} \text{ yr}^{-1}$ (Fox et al. 2014; R17) and the Fermi Bubbles have an outflow rate of $0.2\text{--}0.3 M_{\odot} \text{ yr}^{-1}$ in cool gas (Bordoloi et al. 2017).

4. Discussion and Summary

We have derived new empirical constraints on the mass inflow and outflow rates of cool ionized gas around the MW, by dividing the R17 catalog of 187 UV absorption-line HVCs into inflowing and outflowing populations, and using direct observational constraints on HVC metallicity, dust content, and distance. After removing HVCs associated with the Magellanic Stream and Fermi Bubbles, we find $dM_{\text{in}}/dt \gtrsim (0.53 \pm 0.23)(d/12 \text{ kpc})(Z/0.2Z_{\odot})^{-1} M_{\odot} \text{ yr}^{-1}$ and $dM_{\text{out}}/dt \gtrsim (0.16 \pm 0.07)(d/12 \text{ kpc})(Z/0.5Z_{\odot})^{-1} M_{\odot} \text{ yr}^{-1}$, where we have scaled the results to 20% solar metallicity for the inflow and 50% solar metallicity for the outflow, as HVC observations indicate, and where the uncertainties are formed by propagating the errors discussed in Section 3 on f_{sky} , $\langle N_{\text{H}} \rangle$, $\langle v_{\text{GSR}} \rangle$, and dust depletion (full details on the error propagation are given in the Appendix). If we also propagate the errors on metallicity and distance instead of leaving them as free parameters, we derive final values of $dM_{\text{in}}/dt \gtrsim (0.53 \pm 0.31) M_{\odot} \text{ yr}^{-1}$ and $dM_{\text{out}}/dt \gtrsim (0.16 \pm 0.10) M_{\odot} \text{ yr}^{-1}$, where the “ \gtrsim ” symbol remains because of potential line saturation in Si III 1206.

A comparison of these flow rates shows that: (1) the MW appears to be currently in an inflow-dominated phase, as we observe a net inflow *regardless of HVC distance*, although this is subject to large accumulated uncertainties. Nonetheless, the outflow metallicity would need to be $0.15Z_{\odot}$ for the inflow and outflow rates to match, and such a low value is highly unlikely for a Galactic wind. Furthermore, the excess of inflow over outflow is seen at high significance in the sky covering fractions alone (Table 1). (2) The HVC inflow rate is not sufficient to sustain the Galactic SFR of $1.7 \pm 0.7 M_{\odot} \text{ yr}^{-1}$ (Liquia & Newman 2015) unless hidden saturation of Si III 1206 causes our inflow rate to be

underestimated. If saturation is not the dominant uncertainty, then the inflow metallicity would need to be $0.06Z_{\odot}$ to match the SFR, and such low metallicities are not measured anywhere in the MW gaseous halo. (3) the difference between the mass inflow and outflow rates is largely driven by the difference in metallicity. Put differently, the *metal* inflow and outflow rates in HVCs, $dM_{\text{Z,in}}/dt = (Z/H)_{\text{in}} dM_{\text{in}}/dt$ and $dM_{\text{Z,out}}/dt = (Z/H)_{\text{out}} dM_{\text{out}}/dt$, are statistically indistinguishable: we calculate $dM_{\text{Z,in}}/dt \approx 18 \pm 8 \text{ milli-} M_{\odot} \text{ yr}^{-1}(d/12 \text{ kpc})$ whereas $dM_{\text{Z,out}}/dt \approx 14 \pm 6 \text{ milli-} M_{\odot} \text{ yr}^{-1}(d/12 \text{ kpc})$. These metal fluxes are better known than the mass fluxes because they are independent of metallicity, and simply depend on summing over the observed ionization states of silicon and correcting for dust.

Despite the global excess of inflow, the presence of substantial gas flow in both directions lends support to the presence of a Galactic fountain (Shapiro & Field 1976; Bregman 1980; Houck & Bregman 1990; Spitoni et al. 2008; Kim & Ostriker 2018), in which supernova-driven outflows drive metal-enriched gas $\sim 1\text{--}4 \text{ kpc}$ into the halo before it cools and cycle back to the plane on $\sim 50 \text{ Myr}$ timescales. Other recent observational studies of MW halo absorbers have also found evidence for a fountain scenario (Marasco et al. 2015; Marasco & Fraternali 2017; Werk et al. 2019). Furthermore, our inflow rate of $\gtrsim 0.53 \pm 0.31 M_{\odot} \text{ yr}^{-1}$ matches the rate needed by Galactic chemical evolution models (Chiappini et al. 2001; Chiappini 2009) to explain stellar metal abundance patterns and to resolve the G-dwarf problem, although we caution that the accumulated error on the inflow rate is substantial. This confirms the finding of previous UV surveys that inflowing HVCs trace the replenishment of gas for star formation (Shull et al. 2009; Lehner & Howk 2011; R17).

Our inflow rate of $\gtrsim 0.53 \pm 0.31 M_{\odot} \text{ yr}^{-1}$ is of similar order to earlier UV-based measurements ($\sim 1 M_{\odot} \text{ yr}^{-1}$; Shull et al. 2009; Lehner & Howk 2011; R17), but higher than radio-based measurements derived from large 21 cm HVCs ($\approx 0.08 M_{\odot} \text{ yr}^{-1}$; Putman et al. 2012) and higher than the flow rates derived for individual clouds like Complex C ($\approx 0.1 M_{\odot} \text{ yr}^{-1}$; Wakker et al. 1999; Collins et al. 2003; Shull et al. 2011). This makes sense because most HVC mass is in ionized HVCs (Lehner & Howk 2011). The ratio of the UV inflow rate to the 21 cm inflow rate quantifies the relative mass in ionized and neutral gas. Our inflow rate calculations indicate $\langle N(\text{H II})/N(\text{H I}) \rangle \approx 0.53/0.08 = 6.6$, equivalent to a mean HVC ionization fraction $f_{\text{H II}} = N(\text{H II})/N(\text{H I} + \text{H II}) = 0.87$. This is higher than the mean ionization fraction reported in large 21 cm HVCs such as Complex C and Complex A because such large clouds are atypical; most HVCs are ionized and not detected at 21 cm (Shull et al. 2009; Lehner & Howk 2011; R17).

For comparison with the HVC mass flow rates, the intermediate-velocity mass flow rates are of interest. These can be derived from optical observations of Ca II and Na I absorption (Ben Behkti et al. 2012). The Ca II and Na I doublets are much less saturated than UV resonance lines, particularly at intermediate velocities, resulting in cleaner measurements. Ben Behkti et al. (2012) report a population of Ca II IVCs with a sky covering factor of $\approx 30\%$, a mean $v_{\text{GSR}} = -42 \text{ km s}^{-1}$, and an associated $N(\text{H I})$ distribution peaking near $\log N(\text{H I}) \approx 19$. Combining these numbers with a typical IVC distance of 2 kpc (Richter et al. 2017) we derive an H I mass flow rate of $\approx 0.04 M_{\odot} \text{ yr}^{-1}$ in these Ca II IVCs. If a similar ionization correction $N(\text{H II})/N(\text{H I}) = 6.6$ applies to IVCs as to HVCs, then IVCs represent a total mass flow rate of $\approx 0.27 M_{\odot} \text{ yr}^{-1}$,

comparable to the HVC flow rate (this similarity occurs because the larger column densities of IVCs are compensated by their smaller velocities and distances). To fully explore this, a more thorough investigation of the IVC mass flow rates using UV data would be worthwhile, including a distinction into inflow and outflow and detailed ionization modeling.

We emphasize that the HVC mass flow rates derived in this paper are effectively *instantaneous*, as they represent the mass flux contained in HVCs observed at the current epoch. Hydrodynamic simulations (Heitsch & Putman 2009; Armillotta et al. 2017) show that HVC lifetimes are typically a few 100 Myr depending on HVC mass and the density contrast with the surrounding hot medium, after which the clouds will become disrupted and evaporated by coronal interactions. Caution should therefore be used in integrating our mass flow rates over long timescales to calculate the total mass delivered in and out of the disk, as the gas will change phase over time via evaporation and subsequent condensation (e.g., Fraternali 2017; Voit et al. 2019).

Finally, we can use our HVC mass outflow rate measurement to present the first observational derivation of the mass loading factor of the disk-wide MW wind. We derive $\eta_{\text{HVC}} \gtrsim (0.10 \pm 0.06)(d/12 \text{ kpc})(Z/0.5Z_{\odot})^{-1}$. This matches the predictions from the numerical simulations of feedback by Kim & Ostriker (2018), who find $\eta = 0.1$, but is lower than expectations from chemical evolution modeling; for a MW-type galaxy at $z = 0$, Peebles & Shankar (2011) derive $\eta \approx 1.4$ while Barrera-Ballesteros et al. (2018) derive $\eta \approx 2$. However, our value for η_{HVC} is a lower limit for the same reasons that the mass outflow rate is a lower limit: saturation, ionization effects, and velocity effects. Furthermore, it does not include the contribution of the nuclear wind at the Galactic center. According to biconical outflow modeling of UV absorbers in Fermi Bubble sightlines, the nuclear wind represents a cool gas outflow rate of $0.2\text{--}0.3 M_{\odot} \text{ yr}^{-1}$ (Fox et al. 2015; Bordoloi et al. 2017) and an associated mass loading factor $\eta_{\text{nuclear}} = 0.12\text{--}0.18$. The similarity of the nuclear and disk-wide outflow rates (they agree to within a factor of two) indicates that the Galaxy releases metal-enriched gas into the halo through nuclear feedback *and* disk-wide feedback, and both should

be considered active channels through which it exchanges mass with its environment.

We are grateful to the referee for a constructive report that improved the manuscript. Support for *HST* Archival Program 15020 was provided by NASA through grants from the Space Telescope Science Institute, which is operated by the Association of Universities for Research in Astronomy, Inc., under NASA contract NAS 5-26555. We acknowledge useful conversations on mass flow rates with Josh Peek.

Facility: *HST* (COS).

Appendix Error Analysis







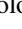

In Table 3 we document the error analysis used to derive the uncertainties on the HVC masses, mass flow rates, metal flow rates, and mass loading factors. The rows in the table show how the percentage errors on each measured quantity (sky covering fraction, mean total silicon column, dust depletion, mean GSR velocity, SFR, metallicity, and distance) propagate to the errors on the derived quantities. The total percentage errors, $\sigma(\text{total})$, are calculated by adding the input percentage errors in quadrature because M , dM/dt , dM_Z/dt , and η_{HVC} are all formed via products and division (Equations (3)–(7)). The dominant error terms are those on the dust, metallicity, and distance, and also SFR, though that only impacts the mass loading factors. The error terms on the covering fractions, mean total silicon column, and mean GSR velocity are much smaller because those quantities are better characterized observationally. We also compute a second total error $\sigma(\text{reduced})$, which is the same as $\sigma(\text{total})$ but without the contribution from the distance and metallicity errors. This is because in the text and in Table 2 we leave distance and metallicity as scalable parameters, so that the equations can be re-evaluated if better constraints become available in the future.

Table 3
Propagation of Errors

Quantity	$\sigma(f_{\text{sky}})$ (%)	$\sigma(\langle N_{\text{Si}} \rangle)$ (%)	$\sigma([\text{Si}/\text{Zn}])$ (%)	$\sigma(\langle v_{\text{GSR}} \rangle)$ (%)	$\sigma(\text{SFR})$ (%)	$\sigma([\text{Si}/\text{H}])$ (%)	$\sigma(d)$ (%)	$\sigma(\text{total})$ (%)	$\sigma(\text{reduced})$ (%)
M_{in}	8	15	38	20	33	66	42
M_{out}	12	20	38	20	33	68	45
dM_{in}/dt	8	15	38	10	...	20	33	58	43
dM_{out}/dt	12	20	38	13	...	20	33	60	46
$dM_{\text{Z,in}}/dt$	8	15	38	10	33	54	43
$dM_{\text{Z,out}}/dt$	12	20	38	13	33	57	46
η_{HVC}	12	20	38	13	40	20	33	72	61

Note. This table reports the percentage errors on the *measured* HVC quantities (sky covering fraction, mean total silicon column, dust depletion, mean GSR velocity, SFR, metallicity, and distance) and how they propagate to the *derived* HVC quantities (masses, mass flow rates, metal flow rates, and mass loading factors). The errors are summed in quadrature following Equations (3)–(7) to form the total error $\sigma(\text{total})$. A second total error $\sigma(\text{reduced})$ is computed *without* the distance and metallicity uncertainties, for use when those two variables are left as scalable parameters. No entry (...) means the variable is not used.

ORCID iDs

Andrew J. Fox  <https://orcid.org/0000-0003-0724-4115>
 Philipp Richter  <https://orcid.org/0000-0002-1188-1435>
 Trisha Ashley  <https://orcid.org/0000-0002-6541-869X>
 Timothy M. Heckman  <https://orcid.org/0000-0001-6670-6370>
 Nicolas Lehner  <https://orcid.org/0000-0001-9158-0829>
 Jessica K. Werk  <https://orcid.org/0000-0002-0355-0134>
 Rongmon Bordoloi  <https://orcid.org/0000-0002-3120-7173>
 Molly S. Peeples  <https://orcid.org/0000-0003-1455-8788>

References

- Armillotta, L., Fraternali, F., Werk, J. K., Prochaska, J. X., & Marinacci, F. 2017, *MNRAS*, **470**, 114
- Barrera-Ballesteros, J. K., Heckman, T., Sánchez, S. F., et al. 2018, *ApJ*, **852**, 74
- Ben Behkhti, N., Winkel, B., Richter, P., et al. 2012, *A&A*, **542**, A110
- Bordoloi, R., Fox, A. J., & Lockman, F. J. 2017, *ApJ*, **831**, 191
- Bregman, J. N. 1980, *ApJ*, **236**, 577
- Brüns, C., Kerp, J., Staveley Smith, L., et al. 2005, *A&A*, **432**, 45
- Chiappini, C. 2009, in IAU Symp. 254, The Galaxy Disk in Cosmological Context, ed. J. Andersen, J. Bland-Hawthorn, & B Nordström (Cambridge: Cambridge Univ. Press), 191
- Chiappini, C., Matteucci, F., & Romano, D. 2001, *ApJ*, **554**, 1044
- Chomiuk, L., & Povich, M. S. 2011, *AJ*, **142**, 197
- Collins, J. A., Shull, J. M., & Giroux, M. L. 2003, *ApJ*, **585**, 336
- Collins, J. A., Shull, J. M., & Giroux, M. L. 2009, *ApJ*, **705**, 962
- D’Onghia, E., & Fox, A. J. 2016, *ARA&A*, **54**, 363
- Diehl, R., Halloin, H., Kretschmer, K., et al. 2006, *Natur*, **439**, 45
- Fielding, D., Quataert, E., & Martizzi, D. 2018, *MNRAS*, **481**, 3325
- Fox, A. J., Bordoloi, R., Savage, B. D., et al. 2015, *ApJL*, **799**, L7
- Fox, A. J., Lehner, N., Lockman, F. J., et al. 2016, *ApJL*, **816**, L11
- Fox, A. J., Richter, P., Wakker, B. P., et al. 2013, *ApJ*, **772**, 110
- Fox, A. J., Savage, B. D., Wakker, B. P., et al. 2004, *ApJ*, **602**, 738
- Fox, A. J., Savage, B. D., & Wakker, B. P. 2006, *ApJS*, **165**, 229
- Fox, A. J., Wakker, B. P., Barger, K. A., et al. 2014, *ApJ*, **787**, 147
- Fraternali, F. 2017, Gas Accretion onto Galaxies, Astrophysics and Space Science Library, Vol. 430 (Cham: Springer), 323
- Gibson, B. K., Giroux, M. L., Penton, S. V., et al. 2001, *AJ*, **122**, 3280
- Green, J. C., Froning, C. S., Osterman, S., et al. 2012, *ApJ*, **744**, 60
- Heitsch, F., & Putman, M. E. 2009, *ApJ*, **698**, 1485
- Herenz, P., Richter, P., Charlton, J. C., & Maseiro, J. R. 2013, *A&A*, **550**, 87
- Houck, J. C., & Bregman, J. N. 1990, *ApJ*, **352**, 506
- Jenkins, E. B. 2009, *ApJ*, **700**, 1299
- Karim, M. T., Fox, A. J., Jenkins, E. B., et al. 2018, *ApJ*, **860**, 98
- Kim, C.-G., & Ostriker, E. C. 2018, *ApJ*, **853**, 173
- Larson, R. B., Tinsley, B. M., & Caldwell, C. N. 1980, *ApJ*, **237**, 692
- Lehner, N., & Howk, J. C. 2010, *ApJL*, **709**, L138
- Lehner, N., & Howk, J. C. 2011, *Sci*, **334**, 955
- Lehner, N., Howk, J. C., Thom, C., et al. 2012, *MNRAS*, **424**, 2896
- Liquia, T. C., & Newman, J. A. 2015, *ApJ*, **806**, 96
- Marasco, A., Debattista, V. P., Fraternali, F., et al. 2015, *MNRAS*, **451**, 4223
- Marasco, A., & Fraternali, F. 2017, *MNRAS*, **464**, L100
- Miville-Deschênes, M.-A., Boulanger, F., Reach, W. T., & Noriega-Crespo, A. 2005, *ApJL*, **631**, L57
- Murphy, E. M., Lockman, F. J., & Savage, B. D. 1995, *ApJ*, **447**, 642
- Nidever, D. L., Majewski, S. R., & Burton, W. B. 2008, *ApJ*, **679**, 432
- Oort, J. H. 1969, *Natur*, **224**, 1158
- Peek, J. E. G., Bordoloi, R., Sana, H., et al. 2016, *ApJL*, **828**, L20
- Peeples, M. S., & Shankar, F. 2011, *MNRAS*, **417**, 2962
- Putman, M. E., Peek, J. E. G., & Jounge, M. R. 2012, *ARA&A*, **50**, 491
- Qu, Z., & Bregman, J. N. 2019, *ApJ*, **880**, 89
- Reid, M. J., Menten, K. M., Brunthaler, A., et al. 2014, *ApJ*, **783**, 130
- Richter, P. 2017, Gas Accretion onto Galaxies, Astrophysics and Space Science Library, Vol. 430 (Cham: Springer), 15
- Richter, P., de Boer, K. S., Werner, K., & Rauch, T. 2015, *A&A*, **584**, L6
- Richter, P., Nuza, S. E., Fox, A. J., et al. 2017, *A&A*, **607**, A48
- Richter, P., Sembach, K. R., Wakker, B. P., et al. 2001a, *ApJ*, **559**, 318
- Richter, P., Sembach, K. R., Wakker, B. P., & Savage, B. D. 2001b, *ApJL*, **562**, 181
- Robitaille, T. P., & Whitney, B. A. 2010, *ApJL*, **710**, L11
- Saul, D. R., Peek, J. E. G., & Putman, M. E. 2014, *MNRAS*, **441**, 2266
- Sembach, K. R., & Savage, B. D. 1996, *ApJ*, **457**, 211
- Sembach, K. R., Wakker, B. P., Savage, B. D., et al. 2003, *ApJS*, **146**, 165
- Shapiro, P. R., & Field, G. B. 1976, *ApJ*, **205**, 762
- Shull, J. M., Jones, J. R., Danforth, C. W., & Collins, J. A. 2009, *ApJ*, **699**, 754
- Shull, J. M., Stevans, M., & Danforth, C. 2011, *ApJ*, **739**, 105
- Smoker, J. V., Fox, A. J., & Keenan, F. P. 2011, *MNRAS*, **415**, 1105
- Spitoni, E., Recchi, S., & Matteucci, F. 2008, *A&A*, **484**, 743
- Tchernyshov, K., Meixner, M., Seale, J., et al. 2015, *ApJ*, **811**, 78
- Thom, C., Peek, J. E. G., Putman, M. E., et al. 2008, *ApJ*, **684**, 364
- Tripp, T. M., Wakker, B. P., Jenkins, E. B., et al. 2003, *AJ*, **125**, 3122
- Tumlinson, J., Peeples, M., & Werk, J. K. 2017, *ARA&A*, **55**, 389
- Voit, G. M., Donahue, M., Zahedy, F., et al. 2019, *ApJL*, **879**, L1
- Wakker, B. P. 2001, *ApJS*, **136**, 463
- Wakker, B. P., & van Woerden, H. 1997, *ARA&A*, **35**, 217
- Wakker, B. P., York, D. G., Wilhelm, R., et al. 2008, *ApJS*, **146**, 1
- Wakker, B. P., et al. 1999, *Natur*, **402**, 388
- Werk, J. K., Rubin, K. H. R., Bish, H. V., et al. 2019, *ApJ*, submitted (arXiv:1904.11014)
- Williams, R. J., Mathur, S., Poindexter, S., Elvis, M., & Nicastro, F. 2012, *AJ*, **143**, 82
- Zech, W. F., Lehner, N., Howk, J. C., Dixon, W. V. D., & Brown, T. M. 2008, *ApJ*, **679**, 460
- Zheng, Y., Peek, J. E. G., Putman, M. E., & Werk, J. K. 2019, *ApJ*, **871**, 35
- Zheng, Y., Putman, M. E., Peek, J. E. G., & Jounge, M. R. 2015, *ApJ*, **807**, 103